RESEARCH ARTICLE

ADVANCED ENERGY MATERIALS
www.advenergymat.de

Co-Free and Ni-Minimized Li- and Mn-Rich Layered Cathodes With Suppressed Structural Disordering for High-Performance and Cost-Effective LIBs

Jinho Ahn, Hyunjin Jang, Hobin Ahn, Hyunji Kweon, Seyeop Oh, Sunha Hwang, Myeong Hwan Lee, Jihyun Hong, and Jongsoon Kim**

The demand for high-performance and cost-effective lithium-ion batteries (LIBs) calls for cathodes with high energy density, structural stability, and reduced reliance on costly Co and Ni. Here, a Co-free and Ni-minimized (≲10 mol%) Li- and Mn-rich layered oxide cathode is presented, $Li_{1.2}Mg_{0.1}Ni_{0.1}Mn_{0.6}O_2$, engineered to balance performance and cost. Low-cost Mg^{2+} substitution can stabilizes the lattice and mitigates voltage decay. However, together with Ni minimization, it suppresses the initial oxygen redox, lowering first-cycle capacity and energy density. Importantly, high-voltage activation during the initial cycle successfully triggers the latent oxygen redox, and remarkably, enables full capacity recovery in subsequent cycles. This pre-activation not only restores performance but also mitigates voltage decay and structural degradation over prolonged cycling. The $Li_{1.2}Mg_{0.1}Ni_{0.1}Mn_{0.6}O_2$ delivers a discharge capacity of ≈276.6 mAh g^{-1} and an energy density of ≈902.2 Wh kg^{-1}, with ≈93.4% capacity retention after 100 cycles. Operando X-ray diffraction reveals a minimal *c*-axis variation (≈0.13%) and provides evidence of suppressed structural disorder following pre-activation. Supported by electrochemical measurements, structural analysis, and first-principles calculations, these findings unlock a pathway toward cost-effective, high-energy layered cathodes with stable cycling performance for next-generation LIBs.

1. Introduction

Lithium-ion batteries (LIBs) offer high energy density and long cycle life for applications ranging from electric vehicles to large-scale energy storage systems,[1–3] thereby motivating intensive efforts toward developing high-capacity cathode materials. Ni-rich layered oxides (NCM, $Li[Ni_xCo_yMn_z]O_2$; $x \geq 0.8$, $x + y + z = 1$) are widely used owing to their high energy density and capacity,[4–6] but their heavy reliance on costly transition metals (TMs, Ni, and Co) raises concerns for large-scale deployment as raw-material costs increasingly dominate the total production cost.[7] As an alternative, Li- and Mn-rich layered oxides (LMROs, $Li_{1+x}TM_{1-x}O_2$) leverage abundant, low-cost Mn and deliver capacities exceeding 250 mAh g^{-1},[8,9] enabled by the combined contributions of cationic and anionic redox. Structurally, excess Li in the TM layers induces in-plane Li/TM ordering and Li–O–Li configurations that activate oxygen redox,[10,11] whereas the large energy separation between Li 1*s* and O 2*p* leaves unhybridized oxygen states near the Fermi level (E_F), thereby facilitating reversible anionic redox reactions.

Despite these advantages, the practical implementation of LMROs still faces serious challenges. When charged to high voltages to fully activate the oxygen redox process, these materials often undergo severe structural degradation, including TM migration, cation disordering, and oxygen release.[12,13] These irreversible changes leads to gradual voltage decay upon prolonged cycling and a pronounced deterioration in cycling stability.

To mitigate these issues, compositional optimization has focused on increasing the fraction of $Li[TM]O_2$-like domains

---

J. Ahn, H. Jang, H. Ahn, H. Kweon, S. Oh, S. Hwang, J. Kim
Department of Energy Science
Sungkyunkwan University
Suwon 16419, Republic of Korea
E-mail: jongsoonkim@skku.edu

The ORCID identification number(s) for the author(s) of this article can be found under https://doi.org/10.1002/aenm.202505121

DOI: 10.1002/aenm.202505121

J. Ahn, H. Jang, H. Ahn, H. Kweon, S. Oh, S. Hwang, J. Kim
SKKU Institute of Energy Science and Technology
Sungkyunkwan University
Suwon 16419, Republic of Korea

M. H. Lee
Advanced Energy Materials Research Center
Korea Research Institute of Chemical Technology (KRICT)
141, Gajeongro, Yuseong, Daejeon 34114, Republic of Korea

J. Hong
Department of Battery Engineering
Graduate Institute of Ferrous & Eco Materials Technology (GIFT)
Pohang University of Science and Technology
Pohang 37673, Republic of Korea
E-mail: jhong@postech.ac.kr

while reducing Li_2MnO_3-like domains to promote reversible TM redox,[14,15] thereby alleviating the irreversible structural degradation originating from oxidized oxygen species in Li_2MnO_3-like domains. However, enlarging the $Li[TM]O_2$-like domains inevitably increases the fraction of expensive TMs. Consequently, various LMRO compositions have been developed to maximize the Ni and Co contents, often exceeding a total of 0.25 mol per formula unit as exemplified by $Li_{1.2}Ni_{0.13}Co_{0.13}Mn_{0.54}O_2$.[16,17] This approach is commonly adopted in studies where considerable amounts of Co ions (> 0.1 mol) are introduced to enhance redox kinetics and cycling stability, particularly when the Ni content exceeds 0.25 mol or when the combined Ni and Co contents surpass that threshold. The presence of Co in LMRO compositions has been reported to enhance redox kinetics and electronic conductivity, which is commonly attributed to the favorable energy alignment between Co $3d$ and O $2p$ orbitals, facilitating orbital hybridization during anionic redox.[18–20]

However, increasing the content of Ni and Co inevitably raises the material cost and compromises the cost-effectiveness of LMROs. LMROs containing substantial Ni and Co ($Ni + Co > 0.25$ mol) often fall short in both cost and performance, as their high contents of Ni and Co undermines the cost advantage, while their electrochemical performance remains inferior to that of Ni-rich NCM cathodes due to limited access to oxygen redox.[21,22] This dual limitation hinders the practical viability of LMROs despite their theoretical advantages. To overcome this challenge, there is a pressing need to develop Co-free, Ni-minimized (≤0.1 mol Ni) LMRO cathodes that retain high capacity and reversibility while significantly reducing the material cost. Despite this need, prior efforts to reduce Ni and Co have explored a wide range of compositions but have not overcome the accompanying losses in performance and structural stability.[23,24] Furthermore, proposed solutions—such as suppressing gas evolution via surface modification[25] and enhancing structural stability by adopting an O2-type stacking order[26]—further complicate implementation. This study aims to address this gap by proposing a new compositional design strategy that maximizes electrochemical performance without relying on expensive TMs.

In this study, we explored the $Li_{1.2}Mg_xNi_{0.2-x}Mn_{0.6}O_2$ compositions to develop Co-free and Ni-minimized LMRO cathodes, since Mg^{2+} is a low-cost element with an ionic radius comparable to that of Ni^{2+}. Moreover, Mg^{2+} exhibits a strong preference for octahedral coordination, which can suppress structural distortions associated with the oxygen redox process.[27,28] However, increasing the Mg^{2+} content in the $Li_{1.2}Mg_xNi_{0.2-x}Mn_{0.6}O_2$ composition enhanced cycle stability but resulted in a considerable decrease in the available capacity. For the Ni-minimized target composition, $Li_{1.2}Mg_{0.1}Ni_{0.1}Mn_{0.6}O_2$ (LMNM-0.1Ni), the first discharge capacity reached only 77.8% of that of $Li_{1.2}Ni_{0.2}Mn_{0.6}O_2$ (LNM-0.2Ni). The reduction in Ni content not only limits the cationic redox contribution but also suppresses the oxygen redox activity, as the decreased electronic conductivity and weakened orbital interactions hinder effective oxygen activation at high voltages.[29–31] Consequently, Li deintercalation from LMNM-0.1Ni during the initial charge becomes restricted compared with LNM-0.2Ni, leading to a significant capacity loss.

To address this, we employed a constant-voltage (CV) charging protocol at 4.7 V during the initial formation step to activate the anionic redox and promote additional Li extraction. As a result, the reversible capacity of LMNM-0.1Ni increased significantly to 276.6 mAh g^{-1}. Remarkably, despite the harsh delithiation conditions, its cycling stability was well maintained, with 93.4% capacity retention over 100 cycles—superior to the 63.2% retention observed for LNM-0.2Ni under the identical conditions.

The electrochemical stabilization of LMNM-0.1Ni is closely linked to its improved structural stability. Notably, operando X-ray diffraction (XRD) revealed a minimal lattice distortion (c-axis variation of ≈0.13%) and an exceptional preservation of Li/TM ordering during cycling, as evidenced by the sustained superlattice reflections—unlike that in LNM-0.2Ni, where these features deteriorate rapidly. This enhanced structural stability, which is rarely observed in LMROs, was further supported by synchrotron-based X-ray absorption spectroscopy (XAS) analysis. Moreover, density functional theory (DFT) calculations confirmed that suppressing both local structural changes and cascade TM migration into Li layers contributes significantly to the observed long-term stability. These results collectively underscore the feasibility of developing Co-free and Ni-minimized (≤0.1 mol Ni) LMROs as structurally stable and high-energy cathodes without relying on expensive TMs.

2. Results and Discussion

2.1. Effect of Ni-Minimization on the Electrochemical Behavior of Co-Free LMROs

To realize high-performance and cost-effective Co-free LMRO cathodes through Ni-minimization, we prepared various $Li_{1.2}Mg_xNi_{0.2-x}Mn_{0.6}O_2$ compositions (x = 0, 0.025, 0.05, 0.1) using the identical solid-state method, as detailed in the Experimental Section. The XRD patterns of all samples are shown in Figure S1 (Supporting Information). All compositions—$Li_{1.2}Ni_{0.2}Mn_{0.6}O_2$ (LNM-0.2Ni), $Li_{1.2}Mg_{0.025}Ni_{0.175}Mn_{0.6}O_2$ (LMNM-0.175Ni), $Li_{1.2}Mg_{0.05}Ni_{0.15}Mn_{0.6}O_2$ (LMNM-0.15Ni) and $Li_{1.2}Mg_{0.1}Ni_{0.1}Mn_{0.6}O_2$ (LMNM-0.1Ni)— exhibited the same layered crystal structure composed of the $R\bar{3}m$ $Li[TM]O_2$-type phase and the monoclinic $C2/m$ Li_2MnO_3-type phase. The characteristic super-structure reflections in the 2θ range of 20–32° indicate the presence of a honeycomb-like in-plane cation ordering of LiM_2 (M = Mn, Ni, and Mg) within the structure,[32] and their intensity and shape remained unchanged with the introduction of Mg. Given that these super-structure reflections are highly sensitive to Li/M ordering, the Mg atoms are likely not segregated in the structure to form Mg-rich regions. No noticeable impurities or second phases were detected in the XRD patterns, indicating the successful preparation of all samples.

These results are consistent with the expected site compatibility between Ni^{2+} and Mg^{2+}, attributed to their similar oxidation states and ionic radii (Mg^{2+}: 0.72 Å / Ni^{2+}: 0.69 Å), which allows Mg-substitution without inducing significant structural distortion. Moreover, scanning electron microscopy (SEM) images revealed that all samples exhibit a comparable morphology and particle size (Figure S2, Supporting Information).

For the Ni-minimized LMNM-0.1Ni, Rietveld refinements were performed on its XRD pattern (**Figure 1a**), yielding lattice parameters for the $R\bar{3}m$ phase ($a = b = 2.8612(2)$ Å and $c = 14.2331(8)$ Å) and the $C2/m$ phase ($a = 5.0393(1)$ Å, $b = 8.4473(3)$ Å, and $c = 4.9800(1)$ Å), respectively. The refined structural

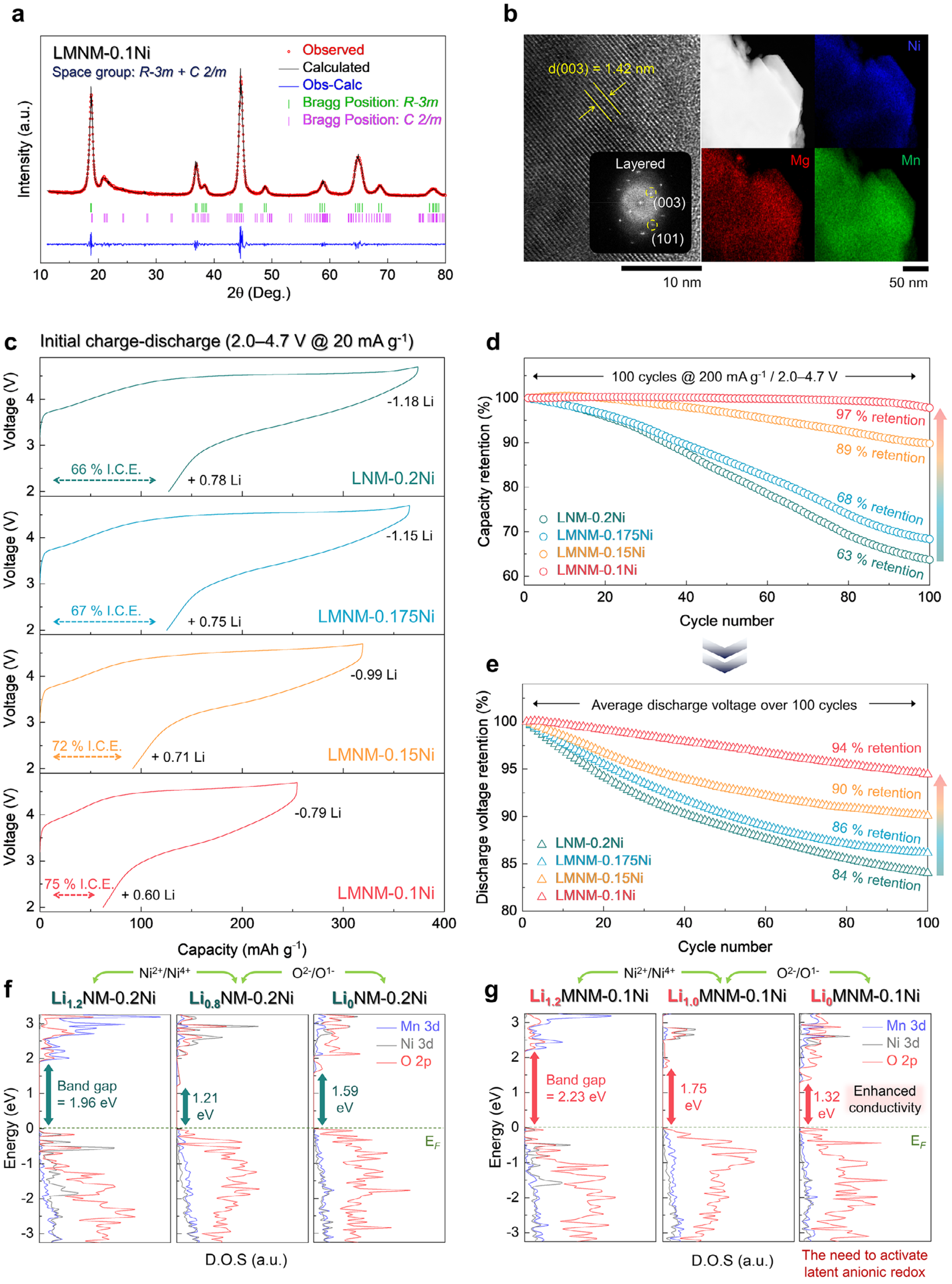

Figure 1. a) Rietveld refinement of XRD pattern, and b) HR-TEM image with corresponding FFT (left) and TEM-EDS mapping (right) of LMNM-0.1Ni. c) Comparison of initial charge/discharge curves in the voltage range of 2.0–4.7 V (versus Li^+/Li) at current density of 20 mA g^{-1}. Comparison of d) discharge capacity retentions and e) discharge voltage retentions over 100 cycles at current density of 200 mA g^{-1}. Calculated pDOS of Mn 3d, Ni 3d, and O 2p orbitals for f) Li_xNM-0.2Ni and g) Li_xMNM-0.1Ni ($0 \leq x \leq 1.2$).

parameters of LMNM-0.1Ni, including atomic coordinates, occupancy, and isotropic temperature factors (B_{iso}), are summarized in Table S1 and S2 (Supporting Information). The refinement results indicate that Mg ions preferentially occupy the TM sites rather than the Li sites. This site preference was further corroborated by DFT calculations. As shown in Figure S3 (Supporting Information), the relative site energies for different Mg positions in the LMNM-0.1Ni structure demonstrate that Mg incorporation into the TM sites is thermodynamically more favorable than into the Li sites.

High-resolution transmission electron microscopy (HR-TEM) analysis revealed that the interlayer spacing of LMNM-0.1Ni was ~1.42 nm, which is consistent with the (003) d-spacing value obtained from the Rietveld refinement (Figure 1b). The fast Fourier transform (FFT) image of the corresponding region confirmed the presence of the (003) and (101) planes of the hexagonal phase, indicating that the LMNM-0.1Ni consists of single-crystalline layered structures. Furthermore, TEM-based elemental mapping conducted via energy-dispersive X-ray spectroscopy (EDS) verified the homogeneous distribution of Ni, Mg, and Mn within the LMNM-0.1Ni particles, with their relative atomic ratios estimated to be approximately 0.1: 0.1: 0.6, in good agreement with the target composition. Inductively coupled plasma atomic emission spectroscopy (ICP-AES) results also showed consistency with the EDS-derived values, further validating the intended stoichiometry of LMNM-0.1Ni (Table S3, Supporting Information). The scanning transmission electron microscopy high-angle annular dark-field (STEM-HAADF) image of LMNM-0.1Ni exhibited uniform contrast without distinct regions, supporting a homogeneous intra-particle compositional distribution (Figure S4, Supporting Information).

To clarify the origin of the capacity decrease upon Ni minimization, we investigated the evolution of both cationic and anionic redox activity through combined experimental and computational analyses. As shown in Figure 1c, we compared the electrochemical performance of LNM-0.2Ni, LMNM-0.175Ni, LMNM-0.15Ni, and LMNM-0.1Ni. According to the initial charge–discharge profiles measured within the voltage range of 2.0–4.7 V (versus Li^+/Li) at a current density of 20 mA g^{-1}, a gradual decrease in capacity was observed with decreasing Ni content. While LNM-0.2Ni delivered an initial discharge capacity of ≈246.6 mAh g^{-1}, LMNM-0.1Ni exhibited a reduced capacity of ≈191.8 mAh g^{-1} under identical conditions. In particular, the initial charge profile of LMNM-0.1Ni showed a significantly shortened high-voltage plateau (≈4.5 V), indicating a suppressed oxygen redox activity compared to LNM-0.2Ni. This suppression is not solely attributed to the reduced cationic redox contribution from Ni but also reflects an intrinsically sluggish oxygen redox kinetics.

Although Ni minimization resulted in a noticeable reduction in specific capacity and energy density, other electrochemical properties showed substantial improvement. Notably, the initial coulombic efficiency increased from ≈66% to ≈75%, indicating that Mg incorporation effectively suppressed irreversible anionic reactions during the first cycle. Most importantly, the cycling stability was significantly enhanced with Ni minimization and Mg substitution: LMNM-0.1Ni retained about 97% of its initial capacity after 100 cycles at 200 mA g^{-1} in the voltage range of 2.0–4.7 V, far outperforming LNM-0.2Ni under identical conditions (Figure 1d; Figure S5, Supporting Information). In addition to the enhanced capacity retention, voltage decay—typically observed during long-term cycling of LMRO cathodes—was substantially mitigated in LMNM-0.1Ni, reflecting an improved stability of the average discharge voltage (Figure 1e).

These improvements are closely associated with the structural stabilization effect of Mg^{2+}, whose fixed valence state ensures that the Mg—O bonds remain chemically inert during electrochemical cycling. This bonding stability effectively suppress local lattice distortions and contributes to the maintenance of the layered framework even under high-voltage oxygen redox conditions. Despite the trade-off in capacity, these results demonstrate that the strategic incorporation of Mg into a Co-free and Ni-minimized LMRO framework yields notable gains in reversibility, voltage stability, and long-term durability—offering a promising pathway toward high-performance and low-cost cathodes for LIBs.

To elucidate the suppressed oxygen redox activity, we compared the ionic and electronic conduction characteristics of LMNM-0.1Ni and LNM-0.2Ni at the onset of the oxygen redox. To simulate the Ni^{4+} oxidation state that initiates anionic redox, we employed the $Li_{1.0}Mg_{0.1}Ni_{0.1}Mn_{0.6}O_2$ ($Li_{1.0}$MNM-0.1Ni) and $Li_{0.8}Ni_{0.2}Mn_{0.6}O_2$ ($Li_{0.8}$NM-0.2Ni) compositions for DFT calculations using the nudged elastic band (NEB) method. As shown in Figure S6 (Supporting Information), the calculations verified that $Li_{1.0}$MNM-0.1Ni exhibits a higher Li^+ migration barrier compared with $Li_{0.8}$NM-0.2Ni. These results indicate that the reduced ionic conductivity in LMNM-0.1Ni collectively hinders oxygen redox kinetics, thereby limiting reversible Li^+ de/intercalation and ultimately causing a more pronounced capacity loss.

In particular, a comparison of the band gap evolution based on the projected density of state (pDOS) analysis supports the differences in electron-transfer kinetics between LMNM-0.1Ni and LNM-0.2Ni (Figure 1f,g).[33,34] The pDOS was calculated using the Heyd–Scuseria–Ernzerhof (HSE06) hybrid functional for more accurate prediction of the anionic redox reaction.[35] The pDOS for pristine state of both materials indicate that LNM-0.2Ni exhibits a narrower band gap of 1.96 eV, while LMNM-0.1Ni shows a wider band gap of 2.23 eV due to weakened orbital hybridization. This trend was maintained in the partially delithiated state, where the Ni^{2+}/Ni^{4+} oxidation was completed, yielding the band gaps of 1.21 eV and 1.75 eV, respectively. Interestingly, at the fully delithiated state, this tendency was reversed. Li_0MNM-0.1Ni exhibits a significantly lower band gap of 1.32 eV compared with 1.59 eV for Li_0NM-0.2Ni. Thus, these pDOS results suggest that the enhanced structural stability induced by Mg-incorporation may initially hinder charge transport, thereby suppressing electrochemical activity in the early states. However, once the anionic redox is activated, the structurally reinforced framework exhibits improved electronic conductivity, suggesting the necessity of employing electrochemical protocols to overcome the initial kinetic limitations of LMNM-0.1Ni.

2.2. Recovery of Oxygen Redox Activity and Enhanced Energy Density via Pre-Activation of Ni-Minimized $Li_{1.2}Ni_{0.1}Mg_{0.1}Mn_{0.6}O_2$ (LMNM-0.1Ni)

In the Ni-minimized LMNM-0.1Ni composition, the initial discharge capacity was significantly lower than that of LNM-0.2Ni. This is primarily attributed to insufficient Li^+ deintercalation during the initial charge, stemming from sluggish oxygen redox kinetics. The reduced Ni content not only limited the cationic redox contribution but also weakened both the electronic and orbital interactions required to support the anionic redox at high voltages, resulting in suppressed participation of oxygen and a lower overall capacity.

To address this limitation, we applied a constant-current/constant-voltage (CC-CV) charging protocol designed to promote further Li deintercalation and to re-activate the latent redox processes. Given that Mg-substitution enhances structural stability and suppresses TM-migration into the Li-layers, we supposed that LMNM-0.1Ni would tolerate high-voltage activation without irreversible degradation. Accordingly, a constant voltage of 4.7 V was applied at the end of the first charge, and the hold time was systematically extended to evaluate the effect of this pre-activation process (**Figure** 2a). Based on the initial dQ/dV profiles (Figure S7, Supporting Information), we set the upper cut-off at 4.7 V—slightly above the anionic reaction shoulder (≈4.59 V) of LMNM-0.1Ni—to ensure sufficient activation. Because LNM-0.2Ni had already extracted ≈1.18 Li per formula unit at 4.7 V, higher voltages would mainly induce side reactions, thus maintaining a constant voltage of 4.7 V enabled a valid comparison between LMNM-0.1Ni and LNM-0.2Ni.

Rather than causing performance degradation, this high-voltage activation resulted in a steady increase in discharge capacity. The specific capacity and energy density of LMNM-0.1Ni increased from approximately 191.8 mAh g^{-1} and 653.4 Wh kg^{-1} to 276.6 mAh g^{-1} and 902.2 Wh kg^{-1}, respectively. When comparing the activation conditions, charging to 4.7 V yielded higher post-activation capacity and energy density than charging to 4.6 V (insufficient Li^+ extraction driving force) or to 4.8 V (enhanced side reactions), identifying 4.7 V as the optimal condition (Figure S8, Supporting Information). Consistent with these improvements, electrochemical impedance spectroscopy (EIS) revealed a reduced charge-transfer resistance (R_{ct}) for the pre-activated LMNM-0.1Ni (≈130 Ω) compared with that of LNM-0.2Ni (≈152 Ω). These results indicate that reactivating latent anionic redox can effectively overcomes the initial kinetic limitations on the basis of its reinforced structural stability (Figure S9, Supporting Information). Furthermore, the pre-activation exerted a beneficial influence on rate performance, enabling higher capacities even at increased current densities (Figure 2b). Most importantly, the enhanced capacity did not come at the expense of long-term stability. After 100 cycles at 200 mA g^{-1}, the pre-activated LMNM-0.1Ni retained 93.4% of its initial capacity, in sharp contrast to that of LNM-0.2Ni, which showed 63.2% retention under identical conditions (Figure 2c; Figure S10, Supporting Information).

In addition to its capacity retention, LMNM-0.1Ni also exhibited a markedly improved voltage stability during cycling. As shown in Figure 2d, the average discharge voltage of LMNM-0.1Ni remained nearly constant throughout 100 cycles, whereas LNM-0.2Ni exhibited a continuous decline with prolonged cycling. This suppression of voltage decay is attributed to the enhanced structural robustness of LMNM-0.1Ni, which preserves the layered framework and mitigates TM migration, typically associated with high-voltage redox reactions. Such a stable voltage profile not only contributes to higher energy output per cycle but also reflects the intrinsic reversibility of its electrochemical processes (Figure 2e,f).

The improved voltage retention of LMNM-0.1Ni was further supported by a differential capacity (dQ/dV) analysis (Figure 2g). LMNM-0.1Ni maintained sharp and well-defined dQ/dV features even after 100 cycles. The peaks retained their original shapes and positions relatively well, indicating suppressed growth of overpotential and enhanced redox reversibility. In contrast, LNM-0.2Ni showed the emergence of a redox peak at ≈2.9 V, attributed to the activation of the Mn^{3+}/Mn^{4+} redox couple. This observation indicates the gradual formation of a spinel-like phase, caused by severe in-plane and out-of-plane TM cation migration. These results provide additional evidence through Mg substitution and Ni minimization effectively mitigates voltage decay and preserves a stable cycling behavior during extended operation.

In addition to these electrochemical benefits, Figure 2h and Figure S11 (Supporting Information) demonstrates that LMNM-0.1Ni achieves an energy density comparable to that of previously reported LMRO compositions containing a high total concentration of TMs (Co + Ni ≥ 0.20 mol), while significantly lowering the use of expensive elements.[36–40] This clearly illustrates the economic advantage of Ni-minimization in terms of energy density-per-cost comparison. Furthermore, when compared to a widely adopted material and Li-free cathode, LMNM-0.1Ni exhibits higher energy density. This result underscores the strong practical competitiveness of LMNM-0.1Ni as a next-generation cathode material capable of delivering both high energy and cost-effectiveness in LIBs.

To assess the practicality of LMNM-0.1Ni in LIBs, we compared the cycle performance of LMNM-0.1Ni and LNM-0.2Ni full cells paired with graphite anodes. After pre-activation at 20 mA g^{-1}, the cells were cycled for 200 cycles at 200 mA g^{-1} within the voltage range of 4.6–1.9 V (Figure S12, Supporting Information). Under these conditions, the LMNM-0.1Ni||graphite full cell retained ~83% of its initial capacity after 200 cycles, whereas the LNM-0.2Ni||graphite full cell retained only ≈27%. These results indicate that LMNM-0.1Ni can deliver more stable electrochemical behavior than LNM-0.2Ni even after pre-activation process at commercial levels.

2.3. Structural Origin of the Stable Cycling Performance in Pre-Activated $Li_{1.2}Ni_{0.1}Mg_{0.1}Mn_{0.6}O_2$ (LMNM-0.1Ni)

Despite the significantly increased capacity and energy density achieved through the pre-activation process, LMNM-0.1Ni maintained excellent long-term cycling stability. To investigate the origin of this structural stability, operando XRD measurements were conducted during the initial charge–discharge process. The results clearly revealed that LMNM-0.1Ni undergoes minimal structural distortion during Li^+ de/intercalation, indicating that the crystal framework remains highly stable even under intensified oxygen redox conditions during the pre-activation process. These results suggest that the improved electrochemical reversibility of LMNM-0.1Ni is closely linked to its intrinsic structural robustness, which effectively suppresses the disordering processes typically triggered by oxygen redox in conventional LMRO cathodes.

As shown in **Figure** 3a,b, LNM-0.2Ni undergoes a series of irreversible phase transitions during the first cycle. The (003) reflection near $2\theta = 18°$ gradually shifts toward lower angles

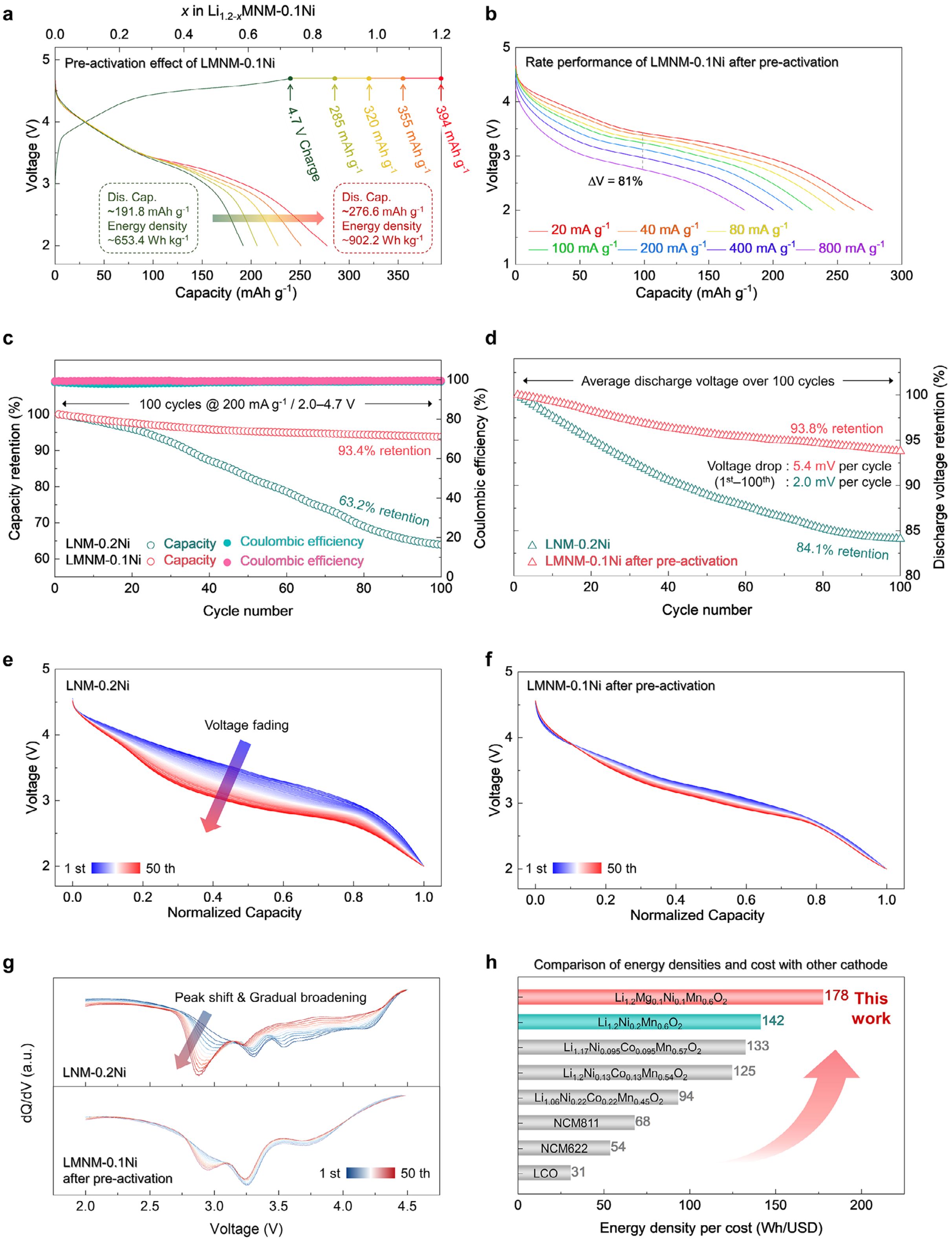

Figure 2. a) Initial charge/discharge profiles of LMNM-0.1Ni under various constant-voltage cut-off conditions at 4.7 V. b) Rate performance of LMNM-0.1Ni evaluated at various discharge current densities after initial pre-activation. Comparison of c) capacity retention and d) discharge voltages retention over 100 cycles at 200 mA g^{-1} between LNM-0.2Ni and LMNM-0.1Ni after pre-activation. Normalized discharge profiles over 50 cycles for e) LNM-0.2Ni and f) pre-activated LMNM-0.1Ni. g) Comparison of dQ/dV discharge profiles of LNM-0.2Ni and LMNM-0.1Ni over 50 cycles. h) Comparison of energy densities and material costs of LMNM-0.1Ni with other reported cathode materials.[36–39]

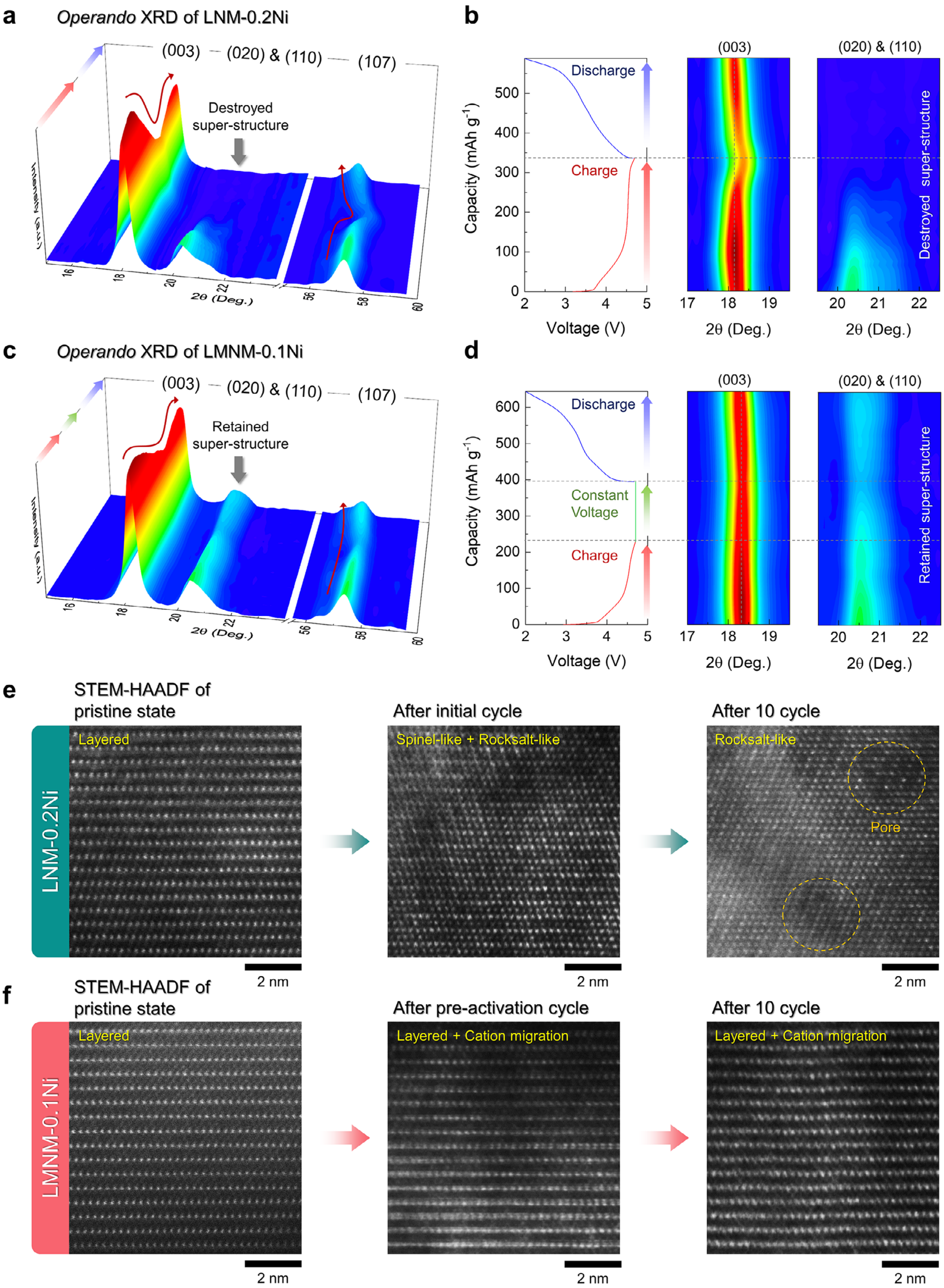

Figure 3. a) Operando XRD and b) magnified 2D contour map of LNM-0.2Ni during the first cycle, overlaid with the voltage profile. c) Operando XRD and d) magnified 2D contour map of LMNM-0.1Ni during the first cycle, overlaid with the voltage profile. e) STEM-HAADF images of LNM-0.2Ni in the pristine state, after initial cycle, and after 10 cycles. Nano-pore formation within particles is highlighted by yellow dotted circles. f) STEM-HAADF images of LMNM-0.1Ni in the pristine state, after pre-activation cycle, and after 10 cycles.

during charging, reflecting *c*-axis expansion due to Li^+ extraction via Ni^{2+}/Ni^{4+} redox. A sharp intensity drop is observed around the high-voltage plateau (≈4.5 V), followed by a sudden peak shift toward higher angles near the end of charge, indicating abrupt lattice contraction caused by slab gliding from O3 to O1-type. Concurrently, the super-lattice reflection associated with in-plane Li/TM ordering, typically located between 20–22°, disappears during charging. This indicates the onset of structural disordering driven by TM migration into Li-layers, a characteristic degradation pathway in the LRMO cathodes.

In contrast, LMNM-0.1Ni exhibits significantly enhanced structural reversibility under identical conditions (Figure 3c,d). The (003) peak shows only slight 2θ shifts (Δc: ≈0.13%) during charge and discharge, and its intensity remains nearly constant, indicating no discernible phase transition. Most notably, the superlattice peaks associated with Li/TM honeycomb ordering are retained throughout the first cycle, even after the forced delithiation imposed by the pre-activation process. This suggests that Mg-substitution effectively suppresses TM migration, thereby stabilizing the cation arrangement within the TM layer and preserving structural integrity during oxygen redox.

Quantitatively, the variation in *c*-lattice parameter for LMNM-0.1Ni during cycling was within 1% (≈0.13%), indicating minimal volume change despite the high degree of Li extraction (Figure S13, Supporting Information). In contrast, LNM-0.2Ni showed significantly greater *c*-axis variation (≈0.31%), highlighting the intrinsic structural instability of the higher-Ni composition. These findings further support the conclusion that the stable cycling behavior of LMNM-0.1Ni originates from its resistance to oxygen redox-induced phase transitions and cation disordering.

The enhanced structural durability of LMNM-0.1Ni was also confirmed by ex situ XRD measurements after prolonged cycling. As shown in Figure S14 (Supporting Information), the major diffraction peaks—(003), (104), and the super-structure reflections—of LMNM-0.1Ni were well preserved even after repeated cycling, whereas those of LNM-0.2Ni showed clear signs of peak broadening and intensity loss. Moreover, ICP-AES elemental analysis after cycling detected no significant decrease in the TM concentration of LMNM-0.1Ni (Table S3, Supporting Information). This comparative analysis further confirms that LMNM-0.1Ni retains its layered structure and long-range ordering more effectively than LNM-0.2Ni.

To further clarify the differences in structural evolution during cycling, STEM-HAADF imaging was conducted to observe atomic-scale structural changes. As shown in Figure 3e, the pristine LNM-0.2Ni exhibits a well-ordered layered structure, although some cation mixing between Ni^{2+} and Li^+ is evident from partial intensity within the Li-layers. Upon repeated cycling, extensive TM migration occurs, resulting in irreversible structural degradation into spinel-like and ultimately rocksalt-like phases. These transitions are accompanied by the collapse of layer ordering and the loss of clear crystallographic separation between the Li and TM layers, as confirmed by inverse FFT analysis (Figure S15, Supporting Information). In addition, localized nanoscale pore formation is observed, likely caused by lattice oxygen release. The progressive loss of structural integrity in LNM-0.2Ni is consistent with the operando XRD results and accounts for the capacity fading and voltage decay observed during electrochemical cycling.

In contrast, LMNM-0.1Ni retains a stable layered framework even after pre-activation and prolonged cycling. As shown in Figure 3f, the pristine LMNM-0.1Ni also displays a typical layered cation arrangement. Although partial cation migration into the Li layers is observed during the high-voltage pre-activation process, the overall layered structure remains intact without significant phase transformation. Even after extended cycling, no clear evidence of spinel or rocksalt phase formation is detected, and the Li/TM layered distinction is well maintained. These observations confirm that Mg substitution effectively inhibits TM migration and structural collapse, even in the presence of activated anionic redox processes.

Overall, the operando XRD and STEM-HAADF results together reinforce the conclusion that the pre-activation strategy in LMNM-0.1Ni enables oxygen redox activation while preserving structural integrity. The suppressed phase transitions, absence of oxygen-induced damage, and retention of layered ordering all contribute to the outstanding long-term electrochemical performance of LMNM-0.1Ni.

2.4. Origin of Suppressed Continuous Cation Migration in Ni-Minimized $Li_{1.2}Ni_{0.1}Mg_{0.1}Mn_{0.6}O_2$ (LMNM-0.1Ni)

To elucidate the origin of the remarkable structural stability observed in LMNM-0.1Ni following high-voltage pre-activation, we conducted DFT calculations to examine the thermodynamics of continuous TM migration. Figure S16 (Supporting Information) presents the typical migration pathway of a TM cation from the initial octahedral site in the TM-layer, through a tetrahedral intermediate, to an adjacent octahedral site in the Li-layer. To evaluate the energetics of this migration process, we modeled fully Li^+ deintercalated $Li_0Ni_{0.2}Mn_{0.6}O_2$ (Li_0NM-0.2Ni) and $Li_0Ni_{0.1}Mg_{0.1}Mn_{0.6}O_2$ (Li_0MNM-0.1Ni) structures, and normalized the site energies of each migration step relative to the initial configuration.

As shown in **Figure 4a**, Ni migration in Li_0NM-0.2Ni induces local decoordination of oxygen and severe distortion of surrounding TMO_6 octahedra, resulting in the formation of a short O═O dimer with a bond length of approximately 1.47 Å. Oxidized oxygen species have a strong driving force to dimerize via O─O covalent bonding, which promotes molecular O_2 evolution and triggers structural collapse. Subsequent Mn migration further shortens the dimer bond length to approximately 1.30 Å and exacerbates local distortion. Importantly, the calculated site energies indicate that each successive migration step lowers the system energy (Figure 4b), confirming that cation migration becomes increasingly favorable as it proceeds. This thermodynamic trend is a key characteristic of structural degradation in in general LMRO cathodes.

In contrast, the Li_0MNM-0.1Ni structure shows strong resistance to TM cation migration. Although initial Ni migration is not thermodynamically favorable, it may be triggered under specific conditions such as the constant voltage activation process. However, in the Mg-substituted structure, subsequent TM migration becomes increasingly unfavorable, thereby suppressing continuous migration and retaining structural

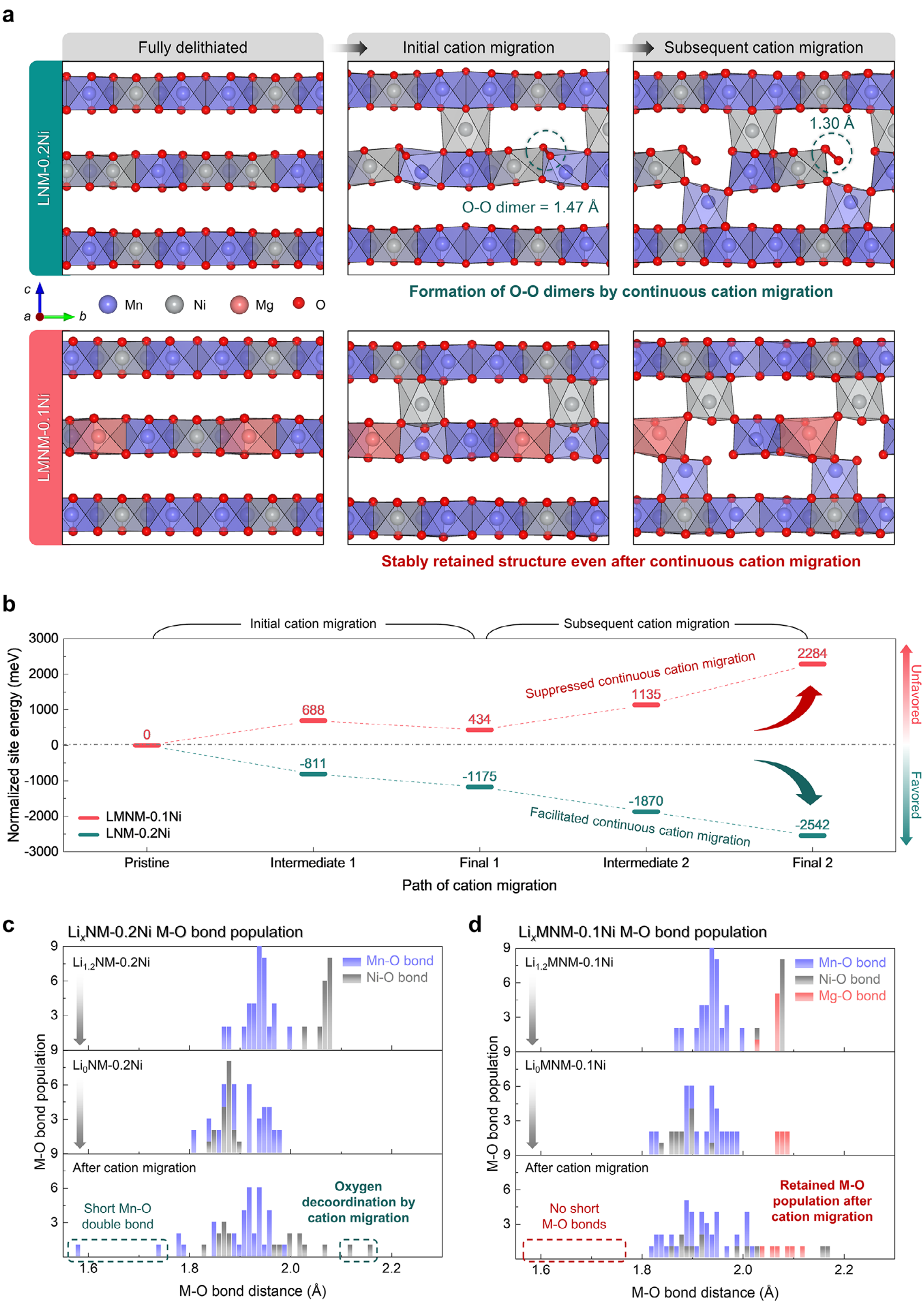

Figure 4. a) Comparison of structural changes in Li$_0$NM-0.2Ni and Li$_0$MNM-0.1Ni under continuous Ni and Mn cation migration steps. O—O dimers formation is highlighted by green dotted circles. b) Relative site energies of intermediate (tetrahedral) and final (octahedral) configurations for Ni and Mn cation migration. Negative energies indicate thermodynamically favorable migration. M—O bond populations for c) LNM-0.2Ni and d) LMNM-0.1Ni in the fully lithiated, fully delithiated, and after cation migration states.

ordering. This behavior is attributed to the structural rigidity of MgO_6 octahedra, which effectively suppresses O═O dimer formation and lattice distortion.[28] The consistently increasing site energies along the migration pathway indicate that significant energy input is required to initiate structural degradation. These results support that, even under forced Li^+ extraction during pre-activation, Li_0MNM-0.1Ni maintains a robust framework that resists cascade-type cation migration, ultimately contributing to the stable cycling performance of LMNM-0.1Ni after the pre-activation process.

To obtain deeper insight into the origin of enhanced structural stability, we compared the evolution of M─O bond lengths during Li^+ extraction and subsequent cation migration in LNM-0.2Ni and LMNM-0.1Ni. As shown in Figure 4c,d, both structures exhibit a same M─O bond distribution in fully Li^+ intercalated state, owing to the chemical similarity between Ni^{2+} and Mg^{2+}. However, upon full delithiation, the contraction of Ni─O and Mn─O bonds is suppressed in $Li_0Mg_{0.1}Ni_{0.1}Mn_{0.6}O_2$ (Li_0MNM-0.1Ni) compared to $Li_0Ni_{0.2}Mn_{0.6}O_2$ (Li_0NM-0.2Ni), due to the rigid Mg–O bonds and the bulky MgO_6 octahedra. Notably, the divergence between two systems becomes more pronounced after cation migration. As observed in Figure 4a above, the migration of cations in Li_0NM-0.2Ni induces severe distortion near the vacant sites, where shortened Mn═O double bonds (≤1.8 Å) and elongated Ni─O bonds (≥2.1 Å) are formed due to the decoordination of oxygen. This rearrangement is thermodynamically favorable because it stabilizes oxidized oxygen by forming O═O dimers via covalent bonding between adjacent oxygen species. The associated oxygen decoordination propagates and promotes further cation migration into vacant sites, accelerating structural degradation. In contrast, Li_0MNM-0.1Ni retains the original M─O bond distribution even after cation migration, thereby suppressing the progression of continuous structural degradation.

The enhanced structural stability of LMNM-0.1Ni was further confirmed through ab initio molecular dynamics (AIMD) simulations. At 750 K for 20 ps, the Li_0NM-0.2Ni structure experienced extensive lattice distortion and spontaneous O_2 evolution (Figure S17, Supporting Information). By contrast, the Li_0MNM-0.1Ni structure maintained its crystalline order under identical conditions without any sign of O_2 release (Figure S18, Supporting Information). These findings suggest that the pre-activation strategy employed for LMNM-0.1Ni can effectively utilize latent anionic redox during the initial cycle to enhance the electrochemical performance. Although partial structural rearrangement occurs, the reinforced structural stability ensures that such changes do not compromise long-term performance.

2.5. Reaction Mechanism and Pre-Activation-Induced Oxygen Redox in Ni-Minimized $Li_{1.2}Ni_{0.1}Mg_{0.1}Mn_{0.6}O_2$ (LMNM-0.1Ni)

The redox reaction in LNM-0.2Ni and LMNM-0.1Ni during Li^+ de/intercalation was confirmed through pDOS calculations. Figure S19 (Supporting Information) shows the pDOS of Ni 3*d*, Mn 3*d* and O 2*p* orbitals in $Li_xNi_{0.2}Mn_{0.6}O_2$ (Li_xNM-0.2Ni) and $Li_xMg_{0.1}Ni_{0.1}Mn_{0.6}O_2$ (Li_xMNM-0.1Ni) with various Li contents ($0 \le x \le 1.2$). Since both materials share identical Ni^{2+}/Ni^{4+} and O^{2-}/O^{1-} redox couples during Li^+ de/intercalation, they exhibit comparable variations in the pDOS. The dominant electron densities of Ni 3*d* orbitals near E_F indicate that Ni^{2+}/Ni^{4+} oxidation is occurred during Li^+ extraction from fully Li^+ intercalated structure. In the $Li_{0.8}$NM-0.2Ni and $Li_{1.0}$MNM-0.1Ni structure, the O 2*p* orbitals exhibited the highest electron density near the E_F, suggesting the presence of non-bonding oxygen states conducive to O^{2-}/O^{1-} oxidation. In the fully delithiated structure, significant hole densities attributed to oxidized oxygen species were observed above the E_F. The electron and hole densities that highlighted in $Li_{1.0}$MNM-0.1Ni and Li_0MNM-0.1Ni were visualized to confirm the anionic redox reaction at atomic level. The occupied electron density (yellow) around oxygen in $Li_{1.0}$MNM-0.1Ni and the emergence hole density (blue) in Li_0MNM-0.1Ni suggest the participation of oxygen in the electrochemical reaction.

To verify the redox reaction occurred in LMNM-0.1Ni during pre-activation process, we performed ex situ synchrotron-based X-ray absorption near edge structure (XANES) and soft X-ray absorption spectroscopy (sXAS) analyses. The Ni K-edge XANES spectra shifted to higher energy during the charging up to 4.4 V and changed in shape upon further charging and pre-activation (**Figure** 5a). Meanwhile, the Mn K-edge XANES spectra exhibited only changes in shape without a significant edge shift during the initial charge/discharge (Figure 5b). These results indicate that the initial Li^+ deintercalation in LMNM-0.1Ni is driven by the Ni^{2+}/Ni^{4+} redox couple, while the subsequent O^{2-}/O^{1-} oxidation at voltage above 4.4 V induces noticeable changes in the spectral shapes of both Ni and Mn K-edges. Notably, similar spectral changes were also observed during the pre-activation step, demonstrating that the capacity originates from forced Li^+ extraction, rather than from electrolyte decomposition. Moreover, the full-discharged LMNM-0.1Ni recovered to a structure closely resembling its original state, with only partial degradation observed.

In the O K-edge region, the pre-edge peak corresponds to the unoccupied TM 3*d*–O 2*p* hybridized states, and its shift toward lower energy is attributed to the increased effective charge of Ni and hole occupancy, as corroborated by the Ni K-edge analysis (Figure 5c). At the full-charged state of 4.7 V, an increase of intensity around ≈530.5 eV was observed, proving the formation of oxidized oxygen species.[41] Furthermore, the intensity in the corresponding region further increased during the pre-activation process in LMNM-0.1Ni, confirming that oxygen participated in the redox reaction for the forced Li^+ deintercalation.

In contrast, the Ni and Mn K-edge XANES spectra of LNM-0.2Ni showed clear evidence of structural degradation. During charging, Li^+ deintercalation proceeds through the same redox couples, Ni^{2+}/Ni^{4+} and O^{2-}/O^{1-} but the spectra after discharged failed to recover their original features. The Mn K-edge spectra shifted to lower energy due to Mn^{3+} reduction, which is attributed to the formation of a rocksalt-like phase induced by TM cation migration. Moreover, the O K-edge sXAS spectra exhibited pronounced changes in the pre-edge peaks corresponding to the t_{2g} and e_g states after the initial cycle, reflecting atomic rearrangements driven by lattice-oxygen release. The emergence of a new peak near 533 eV further indicates the formation of hybridized orbital states associated with Mn^{3+} Jahn-Teller distortion, a characteristic feature of irreversible structural degradation.[42] Moreover, to evaluate the ability to stabilize the lattice oxygen, we compared the amounts of O_2 and CO_2 evolved during the initial charge/discharge

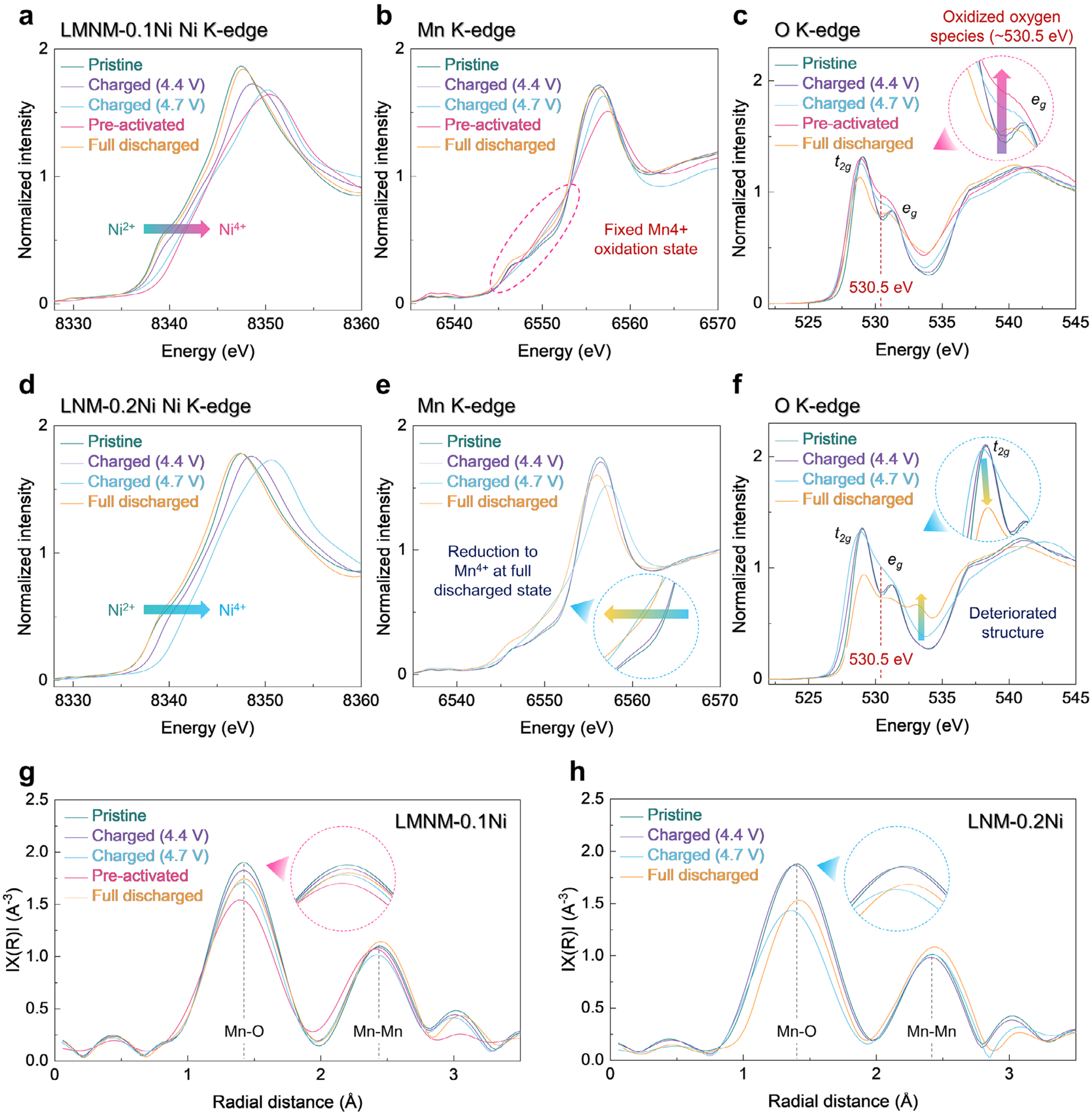

Figure 5. Ex situ analysis of LMNM-0.1Ni: a) Ni K-edge XANES, b) Mn K-edge XANES, and c) O K-edge sXAS spectra. Ex situ analysis of LNM-0.2Ni: d) Ni K-edge XANES, e) Mn K-edge XANES, and f) O K-edge sXAS spectra. Ex situ Mn K-edge EXAFS spectra of g) LMNM-0.1Ni and h) LNM-0.2Ni.

process of LNM-0.2Ni and LMNM-0.1Ni using in situ differential electrochemical mass spectrometry (DEMS). As shown in Figure S20 (Supporting Information), both samples exhibited pronounced CO_2 evolution attributable to the decomposition of the carbonate-based electrolyte.[43,44] Notably, LMNM-0.1Ni displayed negligible O_2 evolution compared with LNM-0.2Ni, indicating that significant lattice-oxygen release and associated structural collapse do not occur even under high-voltage activation conditions.

These XANES results highlighting the differences in local structural evolution between LMNM-0.1Ni and LNM-0.2Ni were further supported by Fourier transformed extended X-ray absorption fine structure (EXAFS) analysis (Figure 5g,h). In the pristine state the Mn K-edge EXAFS spectra of both compositions showed similar peak intensities but clear differences appeared after initial cycling. No significant change was observed during the Ni^{2+}/Ni^{4+} redox process whereas a clear peak shift occurred during the subsequent O^{2-}/O^{1-} oxidation. In LMNM-0.1Ni, a shortening of the Mn─O bond length associated with Li^+ deintercalation was detected during the pre-activation step together with partial intensity loss upon discharge followed by recovery to the original position. In contrast, LNM-0.2Ni showed larger shifts and distortions indicating that the improved local structural stability of LMNM-0.1Ni underlies the effectiveness of the pre-activation strategy.

3. Conclusion

In this study, we proposed a rational design strategy for Co-free and Ni-minimized (≤10 mol%) LMRO cathodes by replacing Ni with low-cost Mg, which offers both chemical similarity and cost-effectiveness. The incorporation of Mg into LNM-0.2Ni to form LMNM-0.1Ni aimed not only to reduce the Ni content but also to enhance tis structural stability. However, the combined effect of Ni minimization and Mg substitution weakened the anionic reaction activity in the initial cycles. This resulted in a low capacity of ≈191.8 mAh g^{-1} and an energy density of ≈653.4 Wh kg^{-1} compared to the conventional LMRO cathode. To overcome this limitation, a high-voltage activation process was employed, which successfully triggered the latent anionic redox activity. Through electrochemical optimization, LMNM-0.1Ni achieved a fully recovered capacity of ≈276.6 mAh g^{-1} and an energy density of ≈902.2 Wh kg^{-1}, comparable to that of conventional LMROs with Ni + Co contents ≥ 20%, but at significantly lower cost. Importantly, LMNM-0.1Ni maintained long-term cycling stability with ≈93.4% retention and exhibited minimal voltage fading even after the pre-activation process. Operando XRD and STEM-HAADF analyses confirmed that the Li/TM ordering was stably preserved throughout the charge/discharge process, with a minimal *c*-axis variation of only ≈0.13%, evidencing superior structural stability. Furthermore, DFT calculations demonstrated that the strong bonding affinity between Mg and O effectively suppresses excessive local structural distortions, thereby preserving structural integrity even upon TM migration to the Li-layers. We believe that our findings provide an effective method to overcome the key challenges in realizing Co-free and Ni-minimized LMRO (≤10 mol%) cathodes, enabling both high electrochemical performance and reduced production cost for next-generation LIBs.

4. Experimental Section

Material Preparation: The $Li_{1.2}Mg_xNi_{0.2\text{-}x}Mn_{0.6}O_2$ ($x = 0$, 0.025, 0.05, and 0.1) systems were synthesized with solid-state method. Stoichiometric amounts of Li_2CO_3 (99%, Alfa aesar), $Ni(OH)_2$ (99%, Alfa aesa), $Mg(OH)_2$ (95%, Samchun), and $MnCO_3$ (99.9%, Alfa aesar) were homogeneously mixed using a planetary ball-milling machine (Pulverisette 6, Fritsch) at 500 rpm for 12 h. After ball-milling, the mixed powder was pelletized and calcined at 800 °C for 1 h with air gas blowing at 3L min^{-1}.

X-Ray Diffraction: XRD data was collected to verify crystal structure using Malvern PANalytical Empyrean with Mo K_α radiation ($\lambda = 0.71$ Å) in the 2θ range of 5–35° with a step size of 0.016°. Rietveld refinement of XRD results was performed to obtain detailed structure information using FullProf software.[45] Operando XRD patterns were obtained at the 3D XRS beamline at the Pohang Accelerator Laboratory (PAL), South Korea, using synchrotron radiation ($\lambda = 0.688314$ Å) with a Mar345 image plate detector in transmission mode and an X-ray exposure time of 3 s. operando XRD was performed during first charge/discharge at a current density of 40 mA g^{-1} in the voltage range of 2.0–4.7 V (versus Li^+/Li). All angles in the XRD data were transformed using Cu K_α radiation ($\lambda = 1.54$ Å) for easy comparison with previous studies.

X-Ray Absorption Spectroscopy: XAS spectra were obtained at beamline 7D XAFS at the PAL, South Korea. The collected data was measured in transmission mode, and reference data were simultaneously collected using Ni and Mn metal foil. Also, O K-edge sXAS spectra were obtained in total fluorescence yield (TFY) mode at beamline 4D-PES at PAL. All of XAS data were normalized using Athena software.[46]

Transmission Electron Microscopy: HR-TEM particle images, atomic-resolution STEM-HAADF images, and EDS elemental maps were obtained using a Cs-corrected microscope (FEI, TITAN TM 80–300) operated at 300 keV. The available point resolution was better than 1 Å at the operating accelerating voltage. Each image was recorded by a 4k × 4k CCD camera (Gatan Oneview 1095).

Differential Electrochemical Mass Spectrometry: The mass spectrometry (HPR-20 R&D, Hiden Analyitical, UK) was used to measure the amounts of O_2 and CO_2 gas evolution during electrochemical test. The gas flow battery cell (GFBC, PDC TECH) was interfaced with the DEMS manifold comprising an Ar carrier gas line, a mass-flow controller, inlet/outlte capillaries. High-purity Ar (99.999%) was used as the carrier at 2 mL min^{-1}. Before measurements, the cell headspace was purged with Ar to remove residual gases, and the cell was cycled between 2.0–4.7 V at a current density of 40 mA g^{-1} while continuously recording the O_2 ($m/z = 32$) and CO_2 ($m/z = 44$) signal.

Electrochemical Characterization: The $Li_{1.2}Mg_xNi_{0.2-x}Mn_{0.6}O_2$ ($x = 0$, 0.02, 0.05, and 0.1) electrode were made by mixing 90 wt% of the active materials, 5 wt% of Super P conductive carbon, and 5 wt% of polyvinylidene fluoride (PVdF). The N-metyhl-2-pyrolidon (NMP) was used as the solvent, and slurry was cast on the Al current collector (15 µm). The electrodes were dried at 100 °C overnight in a vacuum oven. The active mass loading of electrode was ≈2 mg cm^{-2}. The CR-2032 type coin cell was assembled in an Ar filled glovebox. The electrochemical performance was evaluated with a half-cell using Li metal as a counter electrode, separator (Celgard 2400) and 1.2 M $LiPF_6$ in ethylene carbonate (EC): dimethyl carbonate (DMC): ethyl methyl carbonate (EMC) = 2:4:4 (v/v%) as the electrolyte. An automatic charge/discharge system (WBCS 3000, WonATech) was used for galvanostatic charge/discharge test. Power capability of electrodes was tested at various discharge current density (20, 40, 80, 100, 200, 400, and 800 mA g^{-1}) in the voltage range of 2.0–4.7 V (versus Li^+/Li).

Full cells were assembled using commercial graphite (Sigma–Aldrich, powder, < 20 µm) as the anode. The graphite anode slurries were prepared in water with a composition of 90 wt% graphite (active), 4 wt% Super P (conductive carbon), 3 wt% styrene-butadiene rubber (SBR), and 3 wt% carboxymethyl cellulose (CMC), and coated on Cu foil current collector. To reduce the initial irreversibility of graphite, the graphite electrode was pre-cycled by direct contact with Li metal in 1.2 M $LiPF_6$ in EC:EMC:DMC (volume ratio of 2:4:4) electrolyte. Finally, R2032-type full cells were assembled with the LMNM-0.1Ni / LNM-0.2Ni electrode and pre-cycled graphite electrode (capacity ratio of negative and positive electrodes of ≈1.15) in an Ar-filled glove box.

Computational Detail: DFT calculations were performed using the Vienna Ab initio Simulation Package (VASP).[47] Projector-augmented wave pseudopotentials were used with a plane-wave basis set, as implemented in VASP.[48] Perdew-Burke-Ernzerhof (PBE) parametrization of the generalized gradient approximation (GGA) was used for the exchange-correlation functional.[49] For the DFT calculations, a 6 × 3 × 3 k-point grid was used to calculate a 2 x 3 x 1 supercell structure of $Li_{14}Ni_3Mn_7O_{24}$ and $Li_{14}Ni_2Mg_1Mn_7O_{24}$. The GGA+U method was applied to manage the localization of the d-orbital in Ni and Mn ions, with a U value of 6.0 and 3.9 eV, as used in a former study.[50] A kinetic energy cut-off of 500 eV was used in all the converged to within 0.03 eV Å^{-1}. The Heyd–Scuseria–Ernzerhof (HSE06) hybrid functional was applied to accurately calculate the pDOS of Ni, Mn, and O.[35] The crystal structures of calculated configuration were drawn using VESTA software.[51]

The ab initio molecular dynamics (AIMD) simulations were performed based on a Nosé–Hoover thermostat, considering the canonical ensemble as implemented in VASP.[52,53] The projector augmented wave (PAW) potentials and the atomic mass of each element were from the standard VASP library.[54] The simulations were executed at 500 K and 750 K, during 20 ps, taking 2 fs for each time step per ionic step.

Supporting Information

Supporting Information is available from the Wiley Online Library or from the author.

Acknowledgements

This work was supported by the National R&D Program through the National Research Foundation of Korea (NRF) funded by Ministry of Science and ICT (RS-2024-00408156) of Republic of Korea.

Conflict of Interest

The authors declare no conflict of interest.

Data Availability Statement

The data that support the findings of this study are available from the corresponding author upon reasonable request.

Keywords

cathode materials, first-principles calculation, Li-ion batteries, Li-rich layered oxides, Ni minimization

Received: September 11, 2025
Revised: October 15, 2025
Published online: November 10, 2025

[1] X. Zhang, Z. Li, L. Luo, Y. Fan, Z. Du, *Energy* **2022**, *238*, 121652.
[2] S. S. Rangarajan, S. P. Sunddararaj, A. Sudhakar, C. K. Shiva, U. Subramaniam, E. R. Collins, T. Senjyu, *Clean Technol.* **2022**, *4*, 908.
[3] P. Greim, A. A. Solomon, C. Breyer, *Nat. Commun.* **2020**, *11*, 4570.
[4] N. Nasajpour-Esfahani, H. Garmestani, M. Bagheritabar, D. J. Jasim, D. Toghraie, S. Dadkhah, H. Firoozeh, *Renew. Sustain. Energy Rev.* **2024**, *203*, 114783.
[5] G.-T. Park, N.-Y. Park, H.-H. Ryu, H. H. Sun, J.-Y. Hwang, Y.-K. Sun, *Chem. Soc. Rev.* **2024**, *53*, 11462.
[6] S.-B. Lee, N.-Y. Park, G.-T. Park, U.-H. Kim, S.-J. Sohn, M.-S. Kang, R. M. Ribas, R. S. Monteiro, Y.-K. Sun, *ACS Energy Lett.* **2024**, *9*, 740.
[7] S. Jia, W. Meng, S. Li, *Sci. Rep.* **2025**, *15*, 10142.
[8] Y. Lee, H. Park, M. Cho, J. Ahn, W. Ko, J. Kang, Y. J. Choi, H. Kim, I. Park, W. Ryu, J. Hong, J. Kim, *Adv. Funct. Mater.* **2022**, *32*, 2204354.
[9] G. Lim, M. K. Cho, J. Choi, K.-J. Zhou, D. Shin, S. Jeon, M. Kwon, A.-R. Jeon, J. Choi, S. S. Sohn, M. Lee, J. Hong, *Energy Environ. Sci.* **2024**, *17*, 9623.
[10] J. Kim, H. Ahn, J. Ahn, H. Park, J. Hong, M. Hwan Lee, H. Park, J. Kim, *Chem. Eng. J.* **2024**, *495*, 153122.
[11] D. H. Seo, J. Lee, A. Urban, R. Malik, S. Kang, G. Ceder, *Nat. Chem.* **2016**, *8*, 692.
[12] J. Zheng, S. Myeong, W. Cho, P. Yan, J. Xiao, C. Wang, J. Cho, J. Zhang, *Adv. Energy Mater.* **2017**, *7*, 1601284.
[13] S. Cui, M. Gao, G. Li, X. Gao, *Adv. Energy Mater.* **2022**, *12*, 2003885.
[14] K. Luo, M. R. Roberts, N. Guerrini, N. Tapia-Ruiz, R. Hao, F. Massel, D. M. Pickup, S. Ramos, Y.-S. Liu, J. Guo, A. V. Chadwick, L. C. Duda, P. G. Bruce, *J. Am. Chem. Soc.* **2016**, *138*, 11211.
[15] J. Xu, M. Sun, R. Qiao, S. E. Renfrew, L. Ma, T. Wu, S. Hwang, D. Nordlund, D. Su, K. Amine, J. Lu, B. D. McCloskey, W. Yang, W. Tong, *Nat. Commun.* **2018**, *9*, 947.
[16] R. N. Ramesha, D. Bosubabu, M. G. Karthick Babu, K. Ramesha, *ACS Appl. Energy Mater.* **2020**, *3*, 10872, https://doi.org/10.1021/acsaem.0c0189.
[17] K. Redel, A. Kulka, A. Plewa, J. Molenda, *J. Electrochem. Soc.* **2019**, *166*, A5333.
[18] B. Li, Z. Zhuo, L. Zhang, A. Iadecola, X. Gao, J. Guo, W. Yang, A. V. Morozov, A. M. Abakumov, J. M. Tarascon, *Nat. Mater.* **2023**, *22*, 1370.
[19] J. Kou, L. Chen, Y. Su, L. Bao, J. Wang, N. Li, W. Li, M. Wang, S. Chen, F. Wu, *ACS Appl. Mater. Interfaces* **2015**, *7*, 17910.
[20] E. Boivin, N. Guerrini, R. A. House, J. G. Lozano, L. Jin, G. J. Rees, J. W. Somerville, C. Kuss, M. R. Roberts, P. G. Bruce, *Adv. Funct. Mater.* **2021**, *31*, 2003660.
[21] K. I. Hamad, Y. Xing, *J. Electrochem. Soc.* **2018**, *165*, A2470.
[22] W. Li, E. M. Erickson, A. Manthiram, *Nat. Energy* **2020**, *5*, 26.
[23] A. Celeste, M. Tuccillo, A. Santoni, P. Reale, S. Brutti, L. Silvestri, *ACS Appl. Energy Mater.* **2021**, *4*, 11290.
[24] J. Ge, M. Xie, Q. Zhao, S. Zhang, H. Sun, *Int. J. Electrochem. Sci.* **2023**, *18*, 100292.
[25] H. Chen, X. Xia, J. Ma, *ChemSusChem* **2024**, *17*, 202401120.
[26] D. Luo, H. Zhu, Y. Xia, Z. Yin, Y. Qin, T. Li, Q. Zhang, L. Gu, Y. Peng, J. Zhang, K. M. Wiaderek, Y. Huang, T. Yang, Y. Tang, S. Lan, Y. Ren, W. Lu, C. M. Wolverton, Q. Liu, *Nat. Energy* **2023**, *8*, 1078.
[27] J. Ahn, J. Kang, M. Cho, H. Park, W. Ko, Y. Lee, H. Kim, Y. H. Jung, T. Jeon, H. Kim, W. Ryu, J. Hong, J. Kim, *Adv. Energy Mater.* **2021**, *11*, 2102311.
[28] P. K. Nayak, J. Grinblat, E. Levi, M. Levi, B. Markovsky, D. Aurbach, *Phys. Chem. Chem. Phys.* **2017**, *19*, 6142.
[29] C. Yin, L. Wan, B. Qiu, F. Wang, W. Jiang, H. Cui, J. Bai, S. Ehrlich, Z. Wei, Z. Liu, *Energy Storage Mater.* **2021**, *35*, 388.
[30] L. Fang, M. Chen, K.-W. Nam, Y.-M. Kang, *Batteries* **2022**, *8*, 132.
[31] K. Kawai, X.-M. Shi, N. Takenaka, J. Jang, B. M. de Boisse, A. Tsuchimoto, D. Asakura, J. Kikkawa, M. Nakayama, M. Okubo, A. Yamada, *Energy Environ. Sci.* **2022**, *15*, 2591.
[32] Y. S. Meng, G. Ceder, C. P. Grey, W. S. Yoon, M. Jiang, J. Bréger, Y. Shao-Horn, *Chem. Mater.* **2005**, *17*, 2386.
[33] A. J. Garza, G. E. Scuseria, *J. Phys. Chem. Lett.* **2016**, *7*, 4165.
[34] B. Ku, J. Ahn, H. Lee, H. Ahn, J. Lee, H. Kweon, M. Choi, H.-G. Jung, K. Ihm, E. Sim, J.-K. Yoo, J. Kim, *Energy Storage Mater.* **2025**, *74*, 103930.
[35] J. Heyd, G. E. Scuseria, *J. Chem. Phys.* **2004**, *121*, 1187.
[36] C. Yin, Z. Wei, M. Zhang, B. Qiu, Y. Zhou, Y. Xiao, D. Zhou, L. Yun, C. Li, Q. Gu, W. Wen, X. Li, X. Wen, Z. Shi, L. He, Y. Shirley Meng, Z. Liu, *Mater. Today* **2021**, *51*, 15.
[37] S. Kim, W. Cho, X. Zhang, Y. Oshima, J. W. Choi, *Nat. Commun.* **2016**, *7*, 13598.
[38] J. H. Kim, K. J. Park, S. J. Kim, C. S. Yoon, Y. K. Sun, *J. Mater. Chem. A* **2019**, *7*, 2694.
[39] Y. Lyu, X. Wu, K. Wang, Z. Feng, T. Cheng, Y. Liu, M. Wang, R. Chen, L. Xu, J. Zhou, Y. Lu, B. Guo, *Adv. Energy Mater.* **2021**, *11*, 2000982.
[40] X. Pu, J. Heo, J. Yoo, L. Chen, C. Dong, Z. Chen, Y. Cao, J. Peng, R. Li, Y. Yi, K. Kang, Z. Xu, *Adv. Mater.* **2025**, *37*, 07840.
[41] R. A. House, J. J. Marie, M. A. Pérez-Osorio, G. J. Rees, E. Boivin, P. G. Bruce, *Nat. Energy* **2021**, *6*, 781.
[42] N. Ramesh, H. Banerjee, J. E. N. Swallow, E. Björklund, A. Dean, P. Didwal, M. Fraser, C. M. E. Phelan, L. An, J. Singh, J. Lewis, W. Song, R. A. House, A. J. Morris, R. S. Weatherup, R. J. Nicholls, *Chem. Mater.* **2024**, *36*, 11051.

[43] S. L. Dreyer, A. Kondrakov, J. Janek, T. Brezesinski, *J. Mater. Res.* **2022**, *37*, 3146.

[44] J. Rana, J. K. Papp, Z. Lebens-Higgins, M. Zuba, L. A. Kaufman, A. Goel, R. Schmuch, M. Winter, M. S. Whittingham, W. Yang, B. D. McCloskey, L. F. J. Piper, *ACS Energy Lett.* **2020**, *5*, 634.

[45] J. Rodríguez-Carvajal, *Comm. powder Diffr. (IUCr). Newsl.* **2001**, *26*, 12.

[46] B. Ravel, M. Newville, *Phys. Scr.* **2005**, *115*, 1007.

[47] G. Kresse, J. Furthmüller, *Comput. Mater. Sci.* **1996**, *6*, 15.

[48] P. E. Blöchl, *Phys. Rev. B* **1994**, *50*, 17953.

[49] J. P. Perdew, K. Burke, M. Ernzerhof, *Phys. Rev. Lett.* **1996**, *77*, 3865.

[50] A. Jain, G. Hautier, S. P. Ong, C. J. Moore, C. C. Fischer, K. A. Persson, G. Ceder, *Phys. Rev. B* **2011**, *84*, 045115.

[51] K. Momma, F. Izumi, *J. Appl. Crystallogr.* **2008**, *41*, 653.

[52] E. P. Ramos, Z. Zhang, A. Assoud, K. Kaup, F. Lalère, L. F. Nazar, *Chem. Mater.* **2018**, *30*, 7413.

[53] Z. Zhang, P.-N. Roy, H. Li, M. Avdeev, L. F. Nazar, *J. Am. Chem. Soc.* **2019**, *141*, 19360.

[54] G. Kresse, D. Joubert, *Phys. Rev. B* **1999**, *59*, 1758.